ACS OMEGA

http://pubs.acs.org/journal/acsodf

Article

Synthesis, Characterization, and Ionic Conductivity Studies of Simultaneously Substituted K- and Ga-Doped $BaZrO_3$

Akanksha Yadav, Ram Pyare, Thandavarayan Maiyalagan, and Preetam Singh*

Cite This: *ACS Omega* 2021, 6, 30327−30334

Read Online

ACCESS | Metrics & More | Article Recommendations

ABSTRACT: Ceramic fuel cells possess tremendous advantages over PMFCs due to their fuel flexibility and requirement of low-purity hydrogen. Despite high conversion efficiency, the high cost of ultra high-purity hydrogen required for the operation limits the application of PMFCs. Although ceramic fuel cells operate at elevated temperature, high performance coupled with multifuel flexibility makes ceramic fuel cells a superior option as a static power source to generate electricity compared to thermal coal-fired power plants. $BaZr_{1-x}Y_xO_{3-x/2}$ based protonic conductors get a high degree of interest due to their superior structural stability, but their poor conductivity at higher temperature limits the performance of ceramic fuel cells. To overcome the low ionic conductivity issues of $BaZrO_3$ based materials at elevated temperature, the simultaneous doping of smaller Ga on the Zr site and K on the Ba site was employed here to create higher concentration of oxide-ion vacancies for the realization of superior conductivities. The simultaneous substitution of K and Ga created the oxygen vacancy-type point defects resulting in higher ionic conductivity ~10^{-2} S/cm above 650 °C. The conductivity represented here for the $Ba_{0.8}K_{0.2}Zr_{0.8}Ga_{0.2}O_{2.8}$ sample is superior or equivalent to the conductivity obtained for yttria-stabilized zirconia, a well-known ceramic oxide-ion electrolyte.

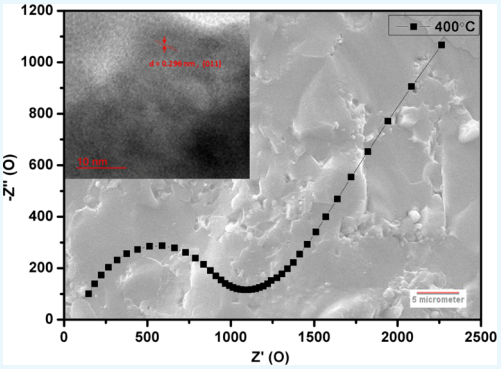

INTRODUCTION

Fuel cells are the electrochemical devices capable of continuously converting the chemical energy stored in a fuel such as hydrogen or methane to electricity.[1,2] Fuel cell technologies can be employed to gradually reduce fossil fuel dependency and environmental impact compared to conventional combustion-based power generation technologies. Ceramic fuel cells generally known as solid oxide fuel cells (SOFCs) use ceramic oxide ion or proton-conducting electrolytes as separators to electrochemically connect the fuel (hydrogen or methane) to oxidant (air or oxygen) to produce electricity. SOFCs operate at higher temperature to avoid the ohmic losses generated due to lower ionic conductivities of electrolyte separators. One of the key approaches to lower the operating temperature of SOFCs is to develop novel electrolyte materials having superior ionic conductivities and thermomechanical properties and low processing temperature compared to those of the well-known perovskite and fluorite-based oxide-ion conductors.[3−6] Perovskites (general formula ABO_3) are a special class of complex oxides that can incorporate a large number of point defects such as oxygen vacancies and protons that compensate dopants or part of inherent off-stoichiometry, and because of this, perovskite-based materials are the most employed host to develop superior ionic conductors. Perovskite oxides with anionic vacancies (inherent or created by doping) perform as oxide-ion conductors in a dry atmosphere at higher temperatures and proton conductors in a hydrated atmosphere at lower operating temperatures.[7−10] Until now, however, only a few materials have been proposed as electrolytes for SOFCs, most of them are simple perovskites suitably doped to get the required oxide-ion vacancies such as Sr- and Mg-doped $LaGaO_3$.[11−14] Commonly used ceramic SOFC electrolytes are Y_2O_3-stabilized ZrO_2,[15,16] gadolinium-doped ceria (GDC),[17] Sm_2O_3-doped CeO_2,[18] scandium-doped zirconia (SDZ),[19] yttrium-stabilized bismuth oxide (BYO),[20] and so forth for oxide-ion conduction.

BaZrO3 is a well-known ceramic that exists in a cubic perovskite structure, which recently gained considerable attention due to its application as a proton-conductor electrolyte in ceramic fuel cells and hydrogen separation membranes with doping of Y on Zr sites.[21,22] The higher protonic conductivity of $BaZr_{1-x}Y_xO_{3-x/2}$ decreases severely at elevated temperature (T > 600 °C) due to its inability to hold

Received: June 14, 2021
Accepted: October 1, 2021
Published: November 1, 2021

moisture/water or adsorbed water from moist air or fuel to retain its protonic conductivity. Due to this, $BaZr_{1-x}Y_xO_{3-x/2}$ has not been found suitable yet as an electrolyte of a fuel cell. High ionic conductivity at elevated temperature ($T > 500$ °C) is a critical requirement for its application as an electrolyte for ceramic fuel cells. Due to high resultant strain on the structure coupled with relatively higher size of Y^{3+} compared to Zr^{4+}, the doping level of Y on the Zr site is kept low, resulting in lower concentration of oxide-ion vacancies, hence lower conductivities by oxide-ion vacancy-type point defects.[23,24]

Oxide-ion conductivity in general gets better at higher temperature in a mobile oxide-ion vacancy conduction model in most of the perovskite- and fluorite-based materials studied so far.[25−30] Therefore, we have envisaged the simultaneous doping of smaller Ga on the Zr site and K on the Ba site to create a higher concentration of oxide-ion vacancies for the realization of superior conductivities. In this manuscript, we are presenting the synthesis, characterization, and ionic conductivity studies of K- and Ga-doped $BaZrO_3$ samples. The higher degree of simultaneous substitution of K and Ga created a higher degree of oxygen vacancy-type point defects, resulting in higher oxide-ion conductivity ~10^{-2} S/cm above 650 °C required for SOFC applications.

EXPERIMENTAL SECTION

Material Synthesis and Characterization. $Ba_{1-x}K_xZr_{1-y}Ga_yO_{3-\delta}$ samples were synthesized by a solid-state ceramic route by mixing a stoichiometric amount of $BaCO_3$, K_2CO_3, ZrO_2, and Ga_2O_3 and subsequently heating them for 15 h at 1150 °C. For obtaining the single-phase material, multiple heating cycles were carried out. Samples were heated thrice at 1150 °C for 15 h with intermediate grounding of the sample. For conductivity measurement, the powder was made into pellets of 10 mm diameter and ~0.2−0.25 cm thickness by pressing it to 6−7 ton weight on a hydraulic press. These pellets were fired at 1200 °C for 10 h for densification. The density of the pellet was measured using the Archimedes method, and it was found to be ~97% of the theoretical density of the material.

The phase formation study was carried out through a Rigaku Miniflex desktop X-ray diffractometer (XRD) with Cu-Kα radiation (λ = 1.54 Å) in the range $2\theta \sim 10-90°$ with a step size of 0.02°. The structures were refined by the Rietveld refinement method using FULLPROF suite software package[31] and cubic perovskite $BaZrO_3$ (space group: $Pm3m$) as the model structure. The microstructures of the sintered samples were investigated using scanning electron microscopy (SEM, EVO—scanning electron microscope MA15/18). The average grain size was calculated using the linear intercept method. The composition of the compounds was examined by energy-dispersive X-ray (EDX) spectroscopy with a probe attached to the SEM instrument.

The total conductivity measurements of all the samples were carried out using an impedance analyzer, AUTOLAB, Netherlands, from 1 MHz to 1 Hz in the temperature range 300−650 °C in different atmospheres. Pt was used as the blocking electrode on both 'opposite' sides of the pellets for conductivity measurements. The total conductivity of the samples is determined from the intercepts of the semicircle on the real axis using the following relationship

$$\sigma = l/RA \text{ S cm}^{-1} \quad (1)$$

where l/A is the geometrical factor, l is the thickness, A is the area of the sample, and R is the total resistance which is indicated by the intercept of the semicircle on the real axis. The sintered pellets were coated with silver paste and cured at 500 °C for 30 min. All measurements were taken during the cooling cycle from 650 to 100 °C.

RESULTS AND DISCUSSION

Up to 25% K at the Ba site and 25% Ga at the Zr site were simultaneously substituted in the $BaZrO_3$ lattice. The synthesized K- and Ga-substituted $BaZrO_3$ powders were off-white, while the undoped $BaZrO_3$ was pure white (Figure 1).

Figure 1. Photograph of synthesized powder (off-white color) and $BaZrO_3$.

The crystal structure and phase purity of the material were studied by powder XRD. The powder XRD patterns of $Ba_{0.9}K_{0.1}Zr_{0.9}Ga_{0.1}O_{2.9}$, $Ba_{0.85}K_{0.15}Zr_{0.85}Ga_{0.15}O_{2.85}$, $Ba_{0.8}K_{0.2}Zr_{0.8}Ga_{0.2}O_{2.8}$, and $Ba_{0.75}K_{0.25}Zr_{0.75}Ga_{0.25}O_{2.75}$ are shown Figure 2b−d, respectively. All the peaks were identified in the $BaZrO_3$ structure (JCPDS no: 98-007-6499). The XRD pattern of most samples (except $Ba_{0.8}K_{0.2}Zr_{0.8}Ga_{0.2}O_{2.8}$) contains the weak reflection for $BaCO_3$ diffraction peaks (JCPDS no: 98-000-5968). Barium is known for very high affinity for CO_2 due to its high basicity. Thus, the minute-level impurity peaks may have arrived due to the presence of some unreacted $BaCO_3$ precursor utilized for the synthesis or formation of $BaCO_3$ on the surface due to CO_2 absorption as all the samples were kept for longer time before we performed the primary XRD study of the materials for comparison. No other reflections can be seen in the powder XRD pattern for any of the Ga_2O_3 and K_2CO_3 phases in $Ba_{1-x}K_xZr_{1-x}Ga_xO_{3-x}$ samples. There is a systematic increase in the lattice parameter of $Ba_{1-x}K_xZr_{1-x}Ga_xO_{3-x}$ with increasing K and Ga content except the x = 0.2 sample that shows the highest conductivity as 2θ shifted to a lower value with the increase in doping concentration (Figure 2f). Crystal structures of K- and Ga-substituted $BaZrO_3$ were refined using the Rietveld method. For this purpose, XRD patterns of the preheated samples were recorded at a slow scan rate of 1° per minute with a 0.01° step size. Figure 3 shows the Rietveld refined XRD profile of (a) $Ba_{0.9}K_{0.1}Zr_{0.9}Ga_{0.1}O_{2.9}$, (b) $Ba_{0.85}K_{0.15}Zr_{0.85}Ga_{0.15}O_{2.85}$, (c) $Ba_{0.8}K_{0.2}Zr_{0.8}Ga_{0.2}O_{2.8}$, and (d) $Ba_{0.75}K_{0.25}Zr_{0.75}Ga_{0.25}O_{2.75}$. The fitted profile matched well with the observed XRD pattern. In the preheated $Ba_{0.75}K_{0.25}Zr_{0.75}Ga_{0.25}O_{3-\delta}$ sample shown in Figure 3d, we still got the weak reflection for the $BaCO_3$ phase (JCPDS no: 98-007-6499) The structural parameters obtained from Reitveld refinement of the powder XRD pattern is given in Table 1. The lattice parameter of $BaZrO_3$ was found to be 4.191 Å, and for $Ba_{0.75}K_{0.25}Zr_{0.75}Ga_{0.25}O_{2.75}$, it was found to be 4.194 Å. The lattice parameter of $Ba_{0.8}K_{0.2}Zr_{0.8}Ga_{0.2}O_{2.8}$ was also found to be

https://doi.org/10.1021/acsomega.1c03110
ACS Omega 2021, 6, 30327−30334

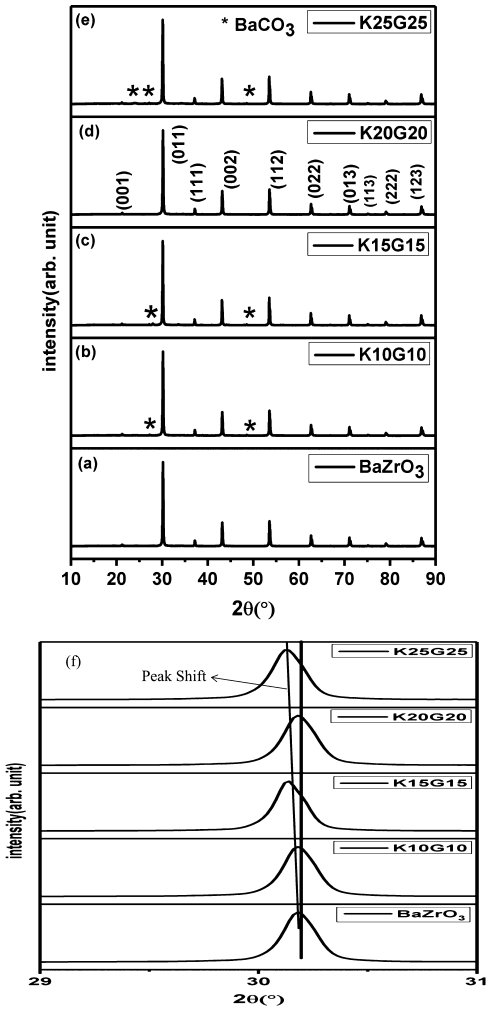

Figure 2. Powder XRD pattern of (a) $BaZrO_3$, (b) $Ba_{0.9}K_{0.1}Zr_{0.9}Ga_{0.1}O_{2.9}$ (K10G10), (c) $Ba_{0.85}K_{0.15}Zr_{0.85}Ga_{0.15}O_{2.85}$ (K15G15), (d) $Ba_{0.8}K_{0.2}Zr_{0.8}Ga_{0.2}O_{2.8}$ (K20G20), and (e) $Ba_{0.75}K_{0.25}Zr_{0.75}Ga_{0.25}O_{2.75}$ (K25G25). (f) Systematic peak shift of the (011) plane of $Ba_{1-x}K_xZr_{1-x}Ga_xO_{3-x}$ (x = 0.0.1, 0.15, 02, and 0.25) samples with doping.

4.1914 Å (higher than the lattice parameter of undoped $BaZrO_3$). The substitution of K^+ and Ga^{3+} on Ba and Zr sites, respectively, in the $BaZrO_3$ lattice shows little increase in the lattice parameter with the increase in doping except the $Ba_{0.8}K_{0.2}Zr_{0.8}Ga_{0.2}O_{2.8}$ sample. A point to be noted is that K^+ ions are slightly greater than Ba^{2+} ions in 12 coordination and Ga^{3+} ions are smaller than Zr^{4+} ions in 6 coordination.[32] Thus, the rigid nature of the octahedral network in the 3-d structure of the perovskite lattice and compensation due to different size cations (K^+ and Ga^{3+} ion substitution in the $BaZrO_3$ lattice) result in only little change in the lattice parameter of doped $BaZrO_3$-based perovskites.

As barium is known to have very high affinity for H_2O and CO_2, TGA/DSC studies were carried out to know the weight loss due to water/moisture absorption and desorption on the materials as well as to know the associated phase changes that may occur due to this. The as-preheated sample of $Ba_{0.8}K_{0.2}Zr_{0.8}Ga_{0.2}O_{2.8}$ was thermally analyzed in thermogravimetric and differential scanning calorimetry (TGA-DSC) analysis at a constant heating rate of 10 °C/min in the temperature range of 30−900 °C. Figure 4 demonstrates the

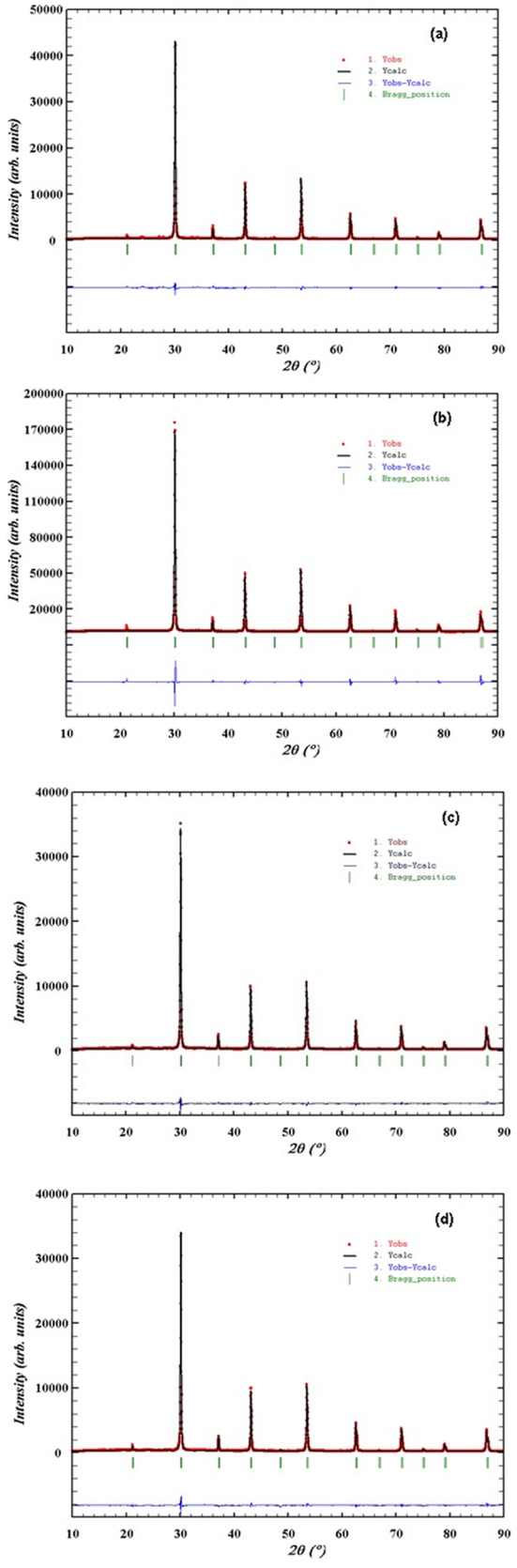

Figure 3. Rietveld refined powder XRD profile of (a) $Ba_{0.9}K_{0.1}Zr_{0.9}Ga_{0.1}O_{2.9}$, (b) $Ba_{0.85}K_{0.15}Zr_{0.85}Ga_{0.15}O_{2.85}$, (c) $Ba_{0.8}K_{0.2}Zr_{0.8}Ga_{0.2}O_{2.8}$, and (d) $Ba_{0.75}K_{0.25}Zr_{0.75}Ga_{0.25}O_{2.75}$.

TGA and DSC curves of the pure $Ba_{0.8}K_{0.2}Zr_{0.8}Ga_{0.2}O_{2.8}$ sample preheated at 200 °C. The first stage of weight loss

https://doi.org/10.1021/acsomega.1c03110
ACS Omega 2021, 6, 30327−30334

Table 1. Structural Parameter of K- and Ga-Doped $BaZrO_3$

compound	lattice parameter (Å) ($a = b = c$)	χ^2	R_f	R_{Bragg}
$BaZrO_3$	4.1910	1.03	2.12	1.04
$Ba_{0.9}K_{0.1}Zr_{0.9}Ga_{0.1}O_{2.9}$	4.1937	3.05	5.14	2.87
$Ba_{0.85}K_{0.15}Zr_{0.85}Ga_{0.15}O_{2.85}$	4.1940	1.46	1.17	1.30
$Ba_{0.8}K_{0.2}Zr_{0.8}Ga_{0.2}O_{2.8}$	4.1914	0.89	1.08	1.26
$Ba_{0.75}K_{0.25}Zr_{0.75}Ga_{0.25}O_{2.75}$	**4.1940**	**4.10**	**4.11**	**1.98**

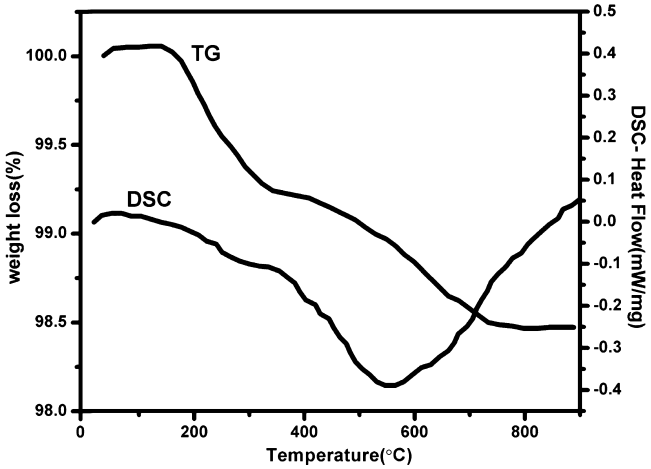

Figure 4. Thermogravimetric analysis (TGA) and DSC curve of $Ba_{0.8}K_{0.2}Zr_{0.8}Ga_{0.2}O_{2.8}$.

between 100 and 200 °C is due to the loss of the adsorbed moisture and structural water present in the sample after exposure to the atmosphere. The second stage of weight loss around 400−600 °C is due to the removal of absorbed or strongly bonded carbonaceous species present in the materials and attributed to the final phase formation. The TGA study confirms the relatively low hygroscopic nature (0.8% weight loss up to 400 °C and total 1.5% weight loss up to 700 °C) of the materials and the absence of absorbed moisture in the sample above 400 °C. The DSC curve shown in Figure 4 does not show any significant feature for any associated phase change that may arrive from oxide-ion vacancy or structure reorientation. Thus, the TGA/DSC studies confirm the structural stability of the material in the temperature range of 30−900 °C.

SEM micrographs of $Ba_{0.8}K_{0.2}Zr_{0.8}Ga_{0.2}O_{2.8}$ (powder, front view, and cross section of the pellet utilized for conductivity measurement) are given in Figure 5a−c. The SEM study reveals that the powder sample contains the dense grains of 3−8 μm in size. No color contrast was observed in the SEM images suggesting the single phase of the materials forming the grains. Figure 5b,c also shows the images of the front and cross section of the pellet. The microstructure of the pellets is showing good density of the pellet, and the grains are in good contact with each other due to crystal growth during sintering. The EDX study with the probe attached to the SEM instrument (micrograph shown in Figure 5d) also confirms that the composition of the materials is close to the nominal composition taken for the synthesis of the material.

TEM investigation of the powder $Ba_{0.8}K_{0.2}Zr_{0.8}Ga_{0.2}O_{2.8}$ sample reveals the presence of agglomeration of particles [Figure 6a,b. In Figure 6c, the electron diffraction image shows the diffraction rings of various planes (011) and (111) that are consistent with XRD indexing of the powder sample (Figure 2). The HRTEM image in Figure 6d] shows that lattice fringes of the sample and the spacing between the adjacent lattice fringes, calculated as 2.96 Å, were assigned to the (011) plane of $Ba_{0.8}K_{0.2}Zr_{0.8}Ga_{0.2}O_{2.8}$. With HRTEM, elemental mapping of the sample $Ba_{0.8}K_{0.2}Zr_{0.8}Ga_{0.2}O_{2.8}$ clearly shows that the sample is composed of Ba, Zr, O, K, and Ga without any impurity elements. EDS mapping ensures that all the elements are

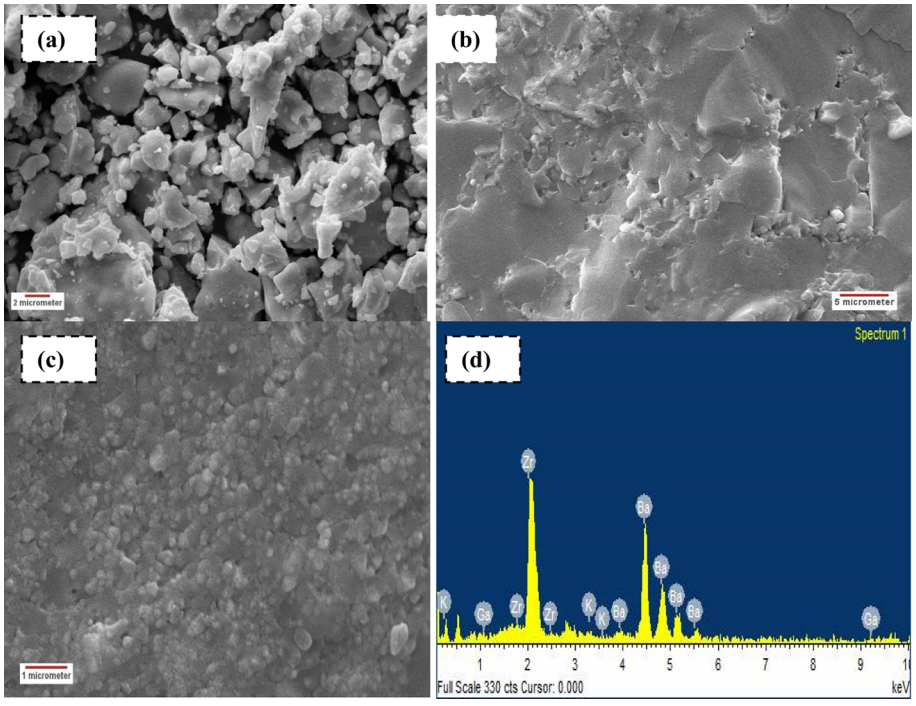

Figure 5. SEM image of $Ba_{0.8}K_{0.2}Zr_{0.8}Ga_{0.2}O_{2.8}$: (a) powder, (b) front view of the pellet, and (c) cross section of the pellets and (d) EDX image of the pellet.

https://doi.org/10.1021/acsomega.1c03110
ACS Omega 2021, 6, 30327−30334

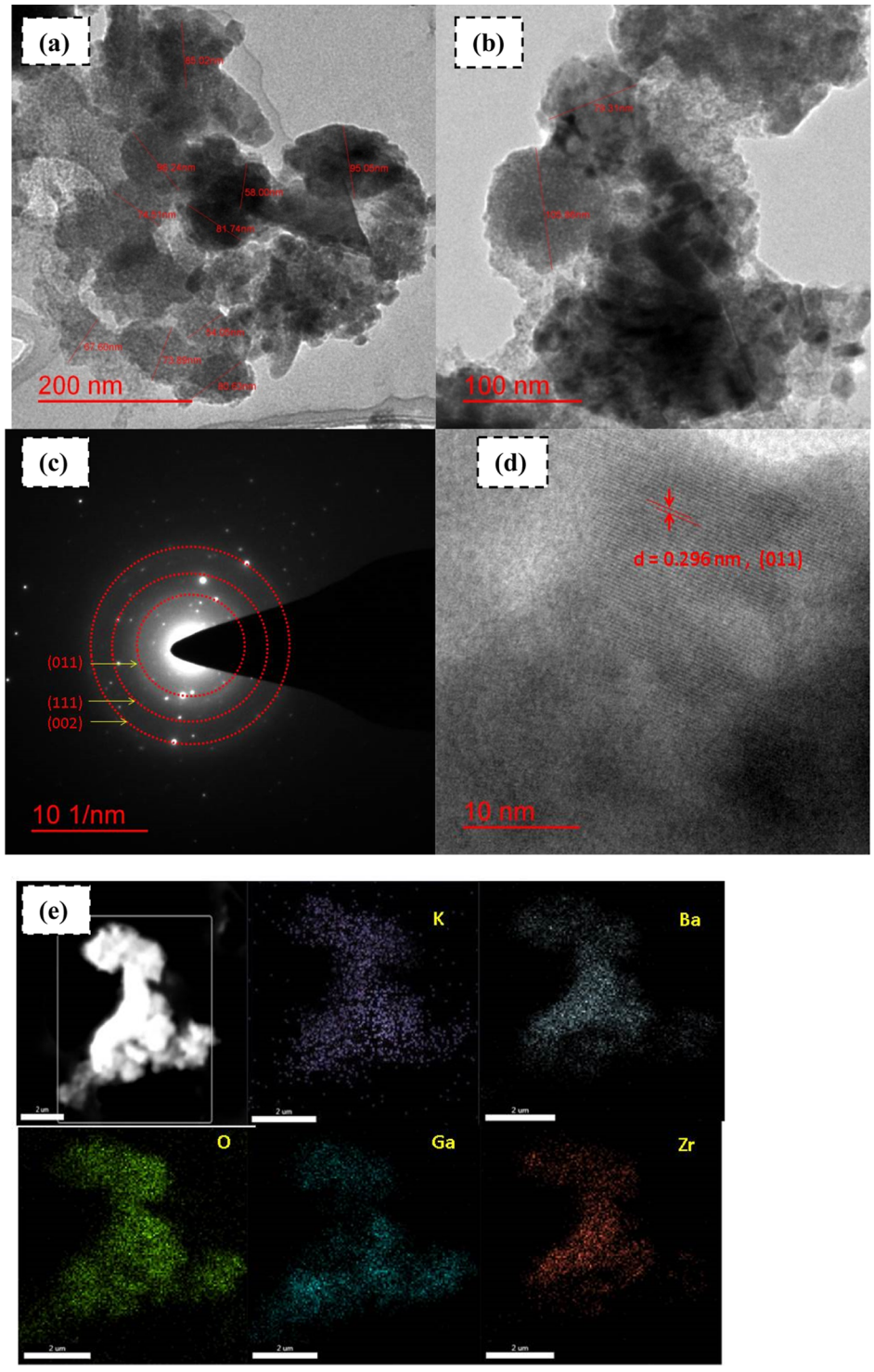

Figure 6. (a,b) TEM image of powder $Ba_{0.8}K_{0.2}Zr_{0.8}Ga_{0.2}O_{2.8}$, (c) SAED pattern from $Ba_{0.8}K_{0.2}Zr_{0.8}Ga_{0.2}O_{2.8}$, (d) HRTEM of $Ba_{0.8}K_{0.2}Zr_{0.8}Ga_{0.2}O_{2.8}$ showing (011) planes, and (e) elemental mapping of $Ba_{0.8}K_{0.2}Zr_{0.8}Ga_{0.2}O_{2.8}$.

uniformly distributed over the cubic structure of nanopowder (Figure 6e). Thus, XRD, SEM, and HRTEM coupled with the EDX study confirm that K^+ and Ga^{3+} ions are substituted in the $BaZrO_3$ lattice, respectively, at Ba^{3+} and Zr^{4+} sites. Considering the Schottky defect formulation, the substitution of K^+ at the Ba^{2+} site and substitution of Ga^{3+} and Zr^{4+} will create oxygen vacancy formation and the defect formation equation using the Kröger–Vink notation can be represented as

$$K'_{Ba} + Ga'_{Zr} \leftrightarrow V_o^{\bullet\bullet}$$

Oxide-ion conductivity or total ionic conductivity studies of the materials were carried out using an impedance spectrometer at various temperatures in different environments. Figure 7a shows the oxide-ion conductivity for different compositions of K- and Ga-substituted $BaZrO_3$, that is, (i) $Ba_{0.9}K_{0.1}Zr_{0.9}Ga_{0.1}O_{2.9}$, (ii) $Ba_{0.85}K_{0.15}Zr_{0.85}Ga_{0.15}O_{2.85}$, (iii) $Ba_{0.8}K_{0.2}Zr_{0.8}Ga_{0.2}O_{2.8}$, and (iv) $Ba_{0.75}K_{0.25}Zr_{0.75}Ga_{0.25}O_{2.75}$.

https://doi.org/10.1021/acsomega.1c03110
ACS Omega 2021, 6, 30327−30334

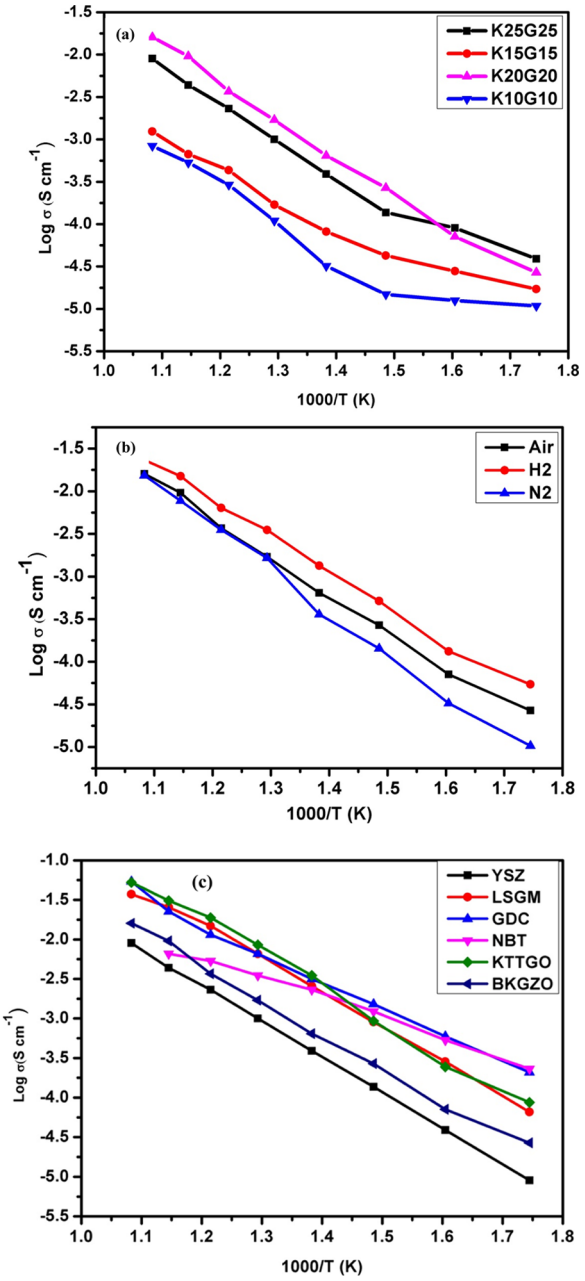

Figure 7. Arrhenius plot of (a) various compositions, (b) $Ba_{0.8}K_{0.2}Zr_{0.8}Ga_{0.2}O_{2.8}$ (BKGZO) in different medium, and (c) comparison of ionic conductivities of the existing intermediate temperature oxide-ion electrolytes in air from refs 21 and 30.

The conductivity was found continuously increasing with increasing temperature for all the compositions. The best oxide-ion conductivity of this series was observed for the composition $Ba_{0.8}K_{0.2}Zr_{0.8}Ga_{0.2}O_{2.8}$, and at 650 °C, the measured oxide-ion conductivity was $\sim 10^{-2}$ S·cm^{-1} for the material. A sudden increase in oxide-ion conductivity was observed over 400 °C of all the samples except $Ba_{0.8}K_{0.2}Zr_{0.8}Ga_{0.2}O_{2.8}$. We also calculated the activation energy of conduction using the Arrhenius equation below 400 °C and above 400 °C. The change in conductivity and activation energy is very similar for the reported perovskite oxide-ion conductors such as $La_{1-x}Sr_xGa_{1-y}Mg_yO_{3-(x+y)/2}$ [11−14] and $Na_{0.5}Bi_{0.5}TiO_3$.[27,28] We believe that in a K- and Ga-doped $BaZrO_3$-based system also, the same mechanism of mobile vacancy percolation is occurring. The conductivity presented here for the $Ba_{0.8}K_{0.2}Zr_{0.8}Ga_{0.2}O_{2.8}$ sample is better or equivalent to the conductivity obtained for yttria-stabilized zirconia (YSZ), a well-known ceramic oxide-ion electrolyte employed for SOFCs. Table 2 presents the conductivities of different compounds that are commonly used as an oxide-ion electrolyte for SOFCs.

Figure 7 shows the Arrhenius plots of total electrical conductivity of $Ba_{1-x}K_xZr_{1-y}Ga_yO_{2-\delta}$ perovskite series with varying potassium and gallium concentration. Here, the conductivity values are plotted against $1000/T$ factor and the slope is calculated by linearly fitting the curve using origin pro software. From the obtained slope, the activation energy is calculated using the following equation

$$\sigma T = \sigma_0 \exp\left(\frac{-E_a}{kT}\right)$$

where σ_0 is the pre-exponential factor, E_a is the activation energy, k is the Boltzman constant, and T is the absolute temperature. The average thickness of each pellet was 0.25 cm. The variation in total conductivity with respect to dopant concentration at various measured temperatures is depicted in Figure 7a. Except the $Ba_{0.8}K_{0.2}Zr_{0.8}Ga_{0.2}O_{2.8}$ sample, two activation regions were found in the K- and Ga-doped BaZrO3 sample as there is a sharp increase in conductivity of all the samples above 400 °C. The activation energy for oxide-ion conductivity was found as low as 0.43 eV for the $Ba_{0.8}K_{0.2}Zr_{0.8}Ga_{0.2}O_{2.8}$ sample. Activation energies for all the samples are provided in Table 3.

Conductivity of $Ba_{0.8}K_{0.2}Zr_{0.8}Ga_{0.2}O_{2.8}$ was also measured in a hydrogen (UHP H_2) and nitrogen (UHP N_2) environment (Figure 7b) to see the effect of absorbed moisture, hydrogen, and oxygen on the surface of the sample. Below 500 °C, the total conductivity of $Ba_{0.8}K_{0.2}Zr_{0.8}Ga_{0.2}O_{2.8}$ was found to be

Table 2. O^{2-} Conductivity (σ) of $Ba_{1-x}K_xZr_{1-y}Ga_yO_{3-\delta}$ at Different Temperatures

	conductivity (S·cm−1)			
compound	650 °C	600 °C	550 °C	500 °C
$Ba_{0.9}K_{0.1}Zr_{0.9}Ga_{0.1}O_{2.9}$	8.6 × 10−4	6.1 × 10−4	2.8 × 10−4	1.6 × 10−4
$Ba_{0.85}K_{0.15}Zr_{0.85}Ga_{0.15}O_{2.85}$	1.1 × 10−3	6.5 × 10−4	4.4 × 10−4	1.6 × 10−4
$Ba_{0.8}K_{0.2}Zr_{0.8}Ga_{0.2}O_{2.8}$	2.1 × 10−2	8.8 × 10−3	3.3 × 10−3	1.6 × 10−3
$Ba_{0.75}K_{0.25}Zr_{0.75}Ga_{0.25}O_{2.75}$	8.9 × 10−3	4.3 × 10−3	2.1 × 10−2	8.9 × 10−4
$KTa_{0.4}Ti_{0.3}Ge_{0.3}O_{2.7}$ (ref 30)	5.2 × 10−2	3.1 × 10−2	9.8 × 10−3	8.5 × 10−3
$Na_{0.5}Bi_{0.49}Ti_{0.98}Mg_{0.02}O_{2.965}$ (ref 21)		6.6 × 10−3	5.4 × 10−3	3.5 × 10−3
$Zr_{0.92}Y_{0.08}O_{1.96}$ (ref 21)		4.4 × 10−3	2.3 × 10−3	1 × 10−3
$Ce_{0.9}Gd_{0.1}O_{1.95}$ (ref 21)		2.3 × 10−2	1.2 × 10−2	6.5 × 10−3
$La_{0.9}Sr_{0.1}Ga_{0.9}Mg_{0.1}O_{2.9}$ (ref 21)		2.5 × 10−2	1.5 × 10−2	6.5 × 10−3

https://doi.org/10.1021/acsomega.1c03110
ACS Omega 2021, 6, 30327−30334

Table 3. Activation Energy of $Ba_{1-x}K_xZr_{1-y}Ga_yO_{3-\delta}$

compound	activation energy (eV)	
	upto 400 °C	above 400 °C
$Ba_{0.9}K_{0.1}Zr_{0.9}Ga_{0.1}O_{2.9}$	2.24	0.48
$Ba_{0.85}K_{0.15}Zr_{0.85}Ga_{0.15}O_{2.85}$	0.45	0.44
$Ba_{0.8}K_{0.2}Zr_{0.8}Ga_{0.2}O_{2.8}$	0.43	0.43
$Ba_{0.75}K_{0.25}Zr_{0.75}Ga_{0.25}O_{2.75}$	1.92	0.47

lower in the nitrogen atmosphere compared to air. This may be due to the fact that some absorbed moisture or hydroxide ions present in the sample can contribute the additional protonic type conductivity at lower temperatures. The higher conductivity above 600 °C (the no weight loss region in TGA, Figure 4) in a nonhumidified environment confirms that the conductivity of the materials at higher temperature is predominantly due to oxide-ion vacancies. Thus, it can be concluded that at temperatures ($T \geq 600$ °C), the ionic conductivity of the material is mainly due to oxide-ion vacancies. The Cole−Cole plot at 500 °C for $Ba_{0.8}K_{0.2}Zr_{0.8}Ga_{0.2}O_{2.8}$ is shown for understanding polarization and to understand the oxide-ion transport nature (Figure 8). Almost linear tails of the Cole−Cole plot at lower frequencies clearly demonstrate ionic contribution in the conductivity.

Hence, it can be concluded that substitutions of K and Ga at Ba and Zr sites, respectively, in the $BaZrO_3$ lattice resulted in stoichiometric oxide-ion vacancy-type point defect formation. The oxide-ion vacancy formation resulted in superior ionic conductivity above 600 °C in nonhumidified atmospheres and helped the material to overcome the poor ionic conductivity problem at elevated temperatures ($T > 500$ °C) which limits the material's application as a conductive electrolyte for ceramic fuel cells. The oxide-ion conductivities obtained here for simultaneously K- and Ga-doped $BaZrO_3$ samples are superior or equivalent to the conductivity obtained for YSZ, a well-known ceramic oxide-ion electrolyte. The present study also opens the doors for employment of novel structural design of materials to generate active oxide-ion vacancies to develop superior ionic conductors. The material can also be explored in a moisture-rich or humidified environment for its applications as a protonic conductor for ceramic fuel cells and hydrogen-separating membrane formations.

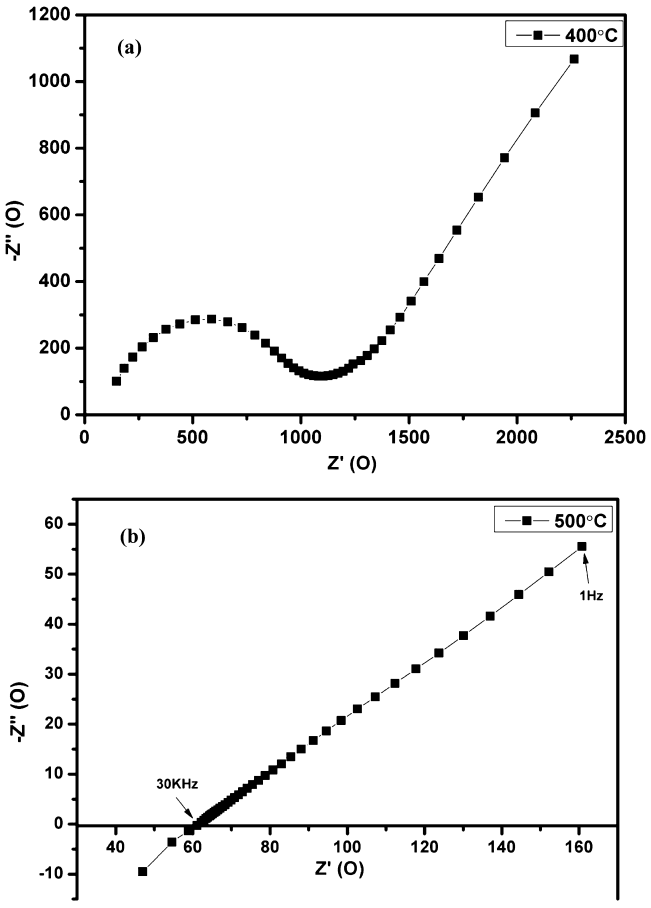

Figure 8. Cole−Cole plot of $Ba_{0.8}K_{0.2}Zr_{0.8}Ga_{0.2}O_{2.8}$ at (a) 400 and (b) 500 °C.

AUTHOR INFORMATION

Corresponding Author

Preetam Singh − *Department of Ceramic Engineering, Indian Institute of Technology (Banaras Hindu University) Varanasi, Varanasi 221005, India;* orcid.org/0000-0002-7590-3576; Phone: 91-947372065; Email: preetamsingh.cer@itbhu.ac.in, preetamchem@gmail.com

Authors

Akanksha Yadav − *Department of Ceramic Engineering, Indian Institute of Technology (Banaras Hindu University) Varanasi, Varanasi 221005, India*

Ram Pyare − *Department of Ceramic Engineering, Indian Institute of Technology (Banaras Hindu University) Varanasi, Varanasi 221005, India*

Thandavarayan Maiyalagan − *Electrochemical Energy Laboratory, Department of Chemistry, SRM Institute of Science and Technology, Kattankulathur 603203 Tamilnadu, India;* orcid.org/0000-0003-3528-3824

Complete contact information is available at: https://pubs.acs.org/10.1021/acsomega.1c03110

Notes

The authors declare no competing financial interest.

ACKNOWLEDGMENTS

Authors thank the Department of Ceramic Engineering, IIT (BHU), for its facility and support. Preetam Singh thanks the Science and Engineering Research Board (SERB) India for the financial support (Project no.: EMR/2016/006840). Akanksha Yadav thanks IIT (BHU) Varanasi for financial support and research fellowship. The authors also thankfully acknowledged the financial support from the Scheme for Promotion of Academic and Research Collaboration (SPARC) of the Ministry of Human Resource Development (MHRD), Government of India, SPARC grant no. SPARC/2018-2019/P1122/SL.

REFERENCES

(1) Stambouli, A. B.; Traversa, E. Solid oxide fuel cells (SOFCs): a review of an environmentally clean and efficient source of energy. *Renew. Sustain. Energy Rev.* **2002**, *6*, 433−455.

(2) Wachsman, E. D.; Lee, K. T. Lowering the Temperature of Solid Oxide Fuel Cells. *Science* **2011**, *334*, 935−939.

(3) Gur, T. M. Comprehensive review of methane conversion in solid oxide fuel cells: Prospects for efficient electricity generation from natural gas. *Energy Combust. Sci.* **2016**, *54*, 1−64.

(4) Gao, Z.; Mogni, L. V.; Miller, E. C.; Railsback, J. G.; Barnett, S. A. A perspective on low-temperature solid oxide fuel cells. *Energy Environ. Sci.* **2016**, *9*, 1602−1644.
(5) Tao, S.; Irvine, J. T. S. A redox-stable efficient anode for solid-oxide fuel cells. *Nat. Mater.* **2003**, *2*, 320−323.
(6) Ruiz-Morales, J. C.; Canales-Vázquez, J.; Savaniu, C.; Marrero-López, D.; Zhou, W.; Irvine, J. T. S. Disruption of extended defects in solid oxide fuel cell anodes for methane oxidation. *Nature* **2006**, *439*, 568−571.
(7) Steele, B. C. H.; Heinzel, A. Materials for fuel-cell technologies. *Nature* **2001**, *414*, 345−352.
(8) Milewski, J.; Miller, A. Influences of The Type and Thickness of Electrolyte on Solid Oxide Fuel Cell Hybrid System Performance. *Trans. ASME* **2006**, *3*, 396−402.
(9) Iwata, M.; Hikosaka, T.; Morita, M.; Iwanari, T.; Ito, K.; Onda, K.; Esaki, Y.; Sakaki, Y.; Nagata, S. Performance analysis of planar-type unit SOFC considering current and temperature distributions. *Solid State Ionics* **2000**, *132*, 297−308.
(10) Minh, N. Q. Ceramic Fuel Cells. *J. Am. Ceram. Soc.* **1993**, *76*, 563−588.
(11) Ishihara, T.; Matsuda, H.; Takita, Y. Doped LaGaO3 Perovskite Type Oxide as a New Oxide Ionic Conductor. *J. Am. Chem. Soc.* **1994**, *116*, 3801−3803.
(12) Huang, K.; Goodenough, J. B. A solid oxide fuel cell based on Sr- and Mg-doped LaGaO3 electrolyte: the role of a rare-earth oxide buffer. *J. Alloys Compd.* **2000**, *303*−*304*, 454−464.
(13) Eba, H.; Anzai, C.; Ootsuka, S. Observation of Cation Diffusion and Phase Formation between Solid Oxide Layers of Lanthanum Gallate-Based Fuel Cells. *Mater. Trans.* **2018**, *59*, 244−250.
(14) Munnings, C. N.; Skinner, S. J.; Amow, G.; Whitfield, P. S.; Davidson, I. J. Stability and reactivity of LSGM electrolytes with nickel-based ceramic cathodes. *J. Fuel Cell Sci. Technol.* **2005**, *2*, 34−37.
(15) Butz, B.; Lefarth, A.; Störmer, H.; Utz, A.; Ivers-Tiffée, E.; Gerthsen, D. Accelerated degradation of 8.5 mol% Y_2O_3-doped zirconia by dissolved Ni. *Solid State Ionics* **2012**, *214*, 37−44.
(16) Balazs, G.; Glass, R. S. AC impedance studies of rare earth oxide doped ceria. *Solid State Ionics* **1995**, *76*, 155−162.
(17) Wang, S.; Kobayashi, T.; Dokiya, M.; Hashimoto, T. Electrical and Ionic Conductivity of Gd-Doped Ceria. *J. Electrochem. Soc.* **2000**, *147*, 3606−3609.
(18) Badwal, S. P. S.; Fini, D.; Ciacchi, F. T.; Munnings, C.; Kimpton, J. A.; Drennan, J. Structural and microstructural stability of ceria - gadolinia electrolyte exposed to reducing environments of high temperature fuel cells. *J. Mater. Chem. A* **2013**, *1*, 10768−10782.
(19) Badwal, S.; Ciacchi, F. T.; Milosevic, D. Scandia-zirconia electrolytes for intermediate temperature solid oxide fuel cell operation. *Solid State Ionics* **2000**, *136*−*137*, 91−99.
(20) Punn, R.; Feteira, A. M.; Sinclair, D. C.; Greaves, C. Enhanced Oxide Ion Conductivity in Stabilized δ-Bi2O3. *J. Am. Chem. Soc.* **2006**, *128*, 15386−15387.
(21) Park, K.-Y.; Seo, Y.; Kim, K. B.; Song, S.-J.; Park, B.; Park, J.-Y. Enhanced proton conductivity of yttrium-doped barium zirconate with sinterability in protonic ceramic fuel cells. *J. Alloys Compd.* **2015**, *639*, 435−444.
(22) Babilo, P.; Uda, T.; Haile, S. M. Processing of Yttrium-doped barium zirconate for high proton conductivity. *J. Mater. Sci.* **2007**, *22*, 1322−1330.
(23) Yamanaka, S.; Fujikane, M.; Hamaguchi, T.; Muta, H.; Oyama, T.; Matsuda, T.; Shin-ichi, K.; Kurosaki, K. Thermophysical properties of $BaZrO_3$ & $BaCeO_3$. *J. Alloys Compd.* **2003**, *359*, 109−113.
(24) Saini, D. S.; Ghosh, A.; Tripathy, S.; Kumar, A.; Sharma, S. K.; Kumar, N.; Majumdar, S.; Bhattacharya, D. A Promising Proton Conducting Electrolyte BaZr1-xHoxO3-δ ($0.05 \leq x \leq 0.20$) Ceramics for Intermediate Temperature Solid Oxide Fuel Cells. *Nat. Sci. Rep.* **2020**, *10*, 3461.
(25) Goodenough, J. B. Oxide-ion conductors by design. *Nature* **2000**, *404*, 821−823.
(26) Skinner, S. J.; Kilner, J. A. Oxygen ion conductors. *Mater. Today* **2003**, *6*, 30−37.
(27) Li, M.; Pietrowski, M. J.; De Souza, R. A.; Huairuo, Z.; Reaney, I. M.; Cook, S. N.; Kilner, J. A.; Sinclair, D. C. A family of oxide ion conductors based on the ferroelectric perovskite $Na_{0.5}Bi_{0.5}TiO_3$. *Nat. Mater.* **2014**, *13*, 31−35.
(28) Yang, F.; Li, M.; Li, L.; Wu, P.; Pradal-Velázque, E.; Sinclair, D. C. Optimisation of oxide-ion conductivity in acceptor-doped Na0.5Bi0.5TiO3 perovskite: approaching the limit? *J. Mater. Chem. A* **2017**, *5*, 21658−21662.
(29) He, X.; Mo, Y. Accelerated materials design of Na0.5Bi0.5TiO3 oxygen ionic conductors based on first principles calculations. *Phys. Chem. Chem. Phys.* **2015**, *17*, 18035−18044.
(30) Yadav, A.; Pyare, R.; Goodenough, J. B.; Singh, P. KTa1-x-yTixGeyO3−δ: A High κ Relaxor Dielectric and Superior Oxide-Ion Electrolyte for IT-SOFC. *ACS Appl. Energy Mater.* **2020**, *3*, 3205−3211.
(31) Rodriguez-Carvajal, J. *Multipattern RietVeld Refinement Program FullProf 2k*, version 3.30; Laboratiore Léon Brillouin: CEA: Saclay, France, 2005.
(32) Shannon, R. D. Revised Effective Ionic Radii and Systematic Studies of Interatomic Distances in Halides and Chalcogenides. *Acta Crystallogr., Sect. A: Cryst. Phys., Diffr., Theor. Gen. Crystallogr.* **1976**, *32*, 751−767.

https://doi.org/10.1021/acsomega.1c03110
ACS Omega 2021, 6, 30327−30334